International Journal of
INTELLIGENT SYSTEMS AND APPLICATIONS IN ENGINEERING
ISSN:2147-6799 www.ijisae.org Original Research Paper

A Decision Support System for Kidney Cancer Detection in Renal Images Using Deep Learning Models

Ahmed Al-Khayyat, Ibraheem Kasim Ibraheem

Submitted: 23/05/2023 **Revised:** 08/07/2023 **Accepted:** 25/07/2023

Abstract:

Kidney cancer comes in various kinds where. Renal Cell Carcinoma (RCC) is the most severe as well as common sort of cancer, which is accountable for around 85% of adults. The earlier diagnosis of kidney cancer has enormous advantages in producing preventive measures that reduce the effect, reduce death rates, and overcome the tumor. Manually detecting whole slide images (WSI) of renal tissues is a basic RCC prognosis and diagnosis device. However, manual analysis of RCC is disposed to inter-subject variability and is time-consuming. Compared to the time-consuming and tedious classical diagnoses, the automatic detection algorithm of deep learning (DL) could improve test accuracy, save diagnoses time, reduce the radiologist's workload, and reduce costs. The study presents a Computational Intelligence with a Deep Learning Decision Support System for Kidney Cancer (CIDL-DSSKC) technique on renal images. The presented CIDL-DSSKC model observes the renal imageries for identifying and recognizing kidney cancer. The presented CIDL-DSSKC method uses Median and Wiener filters for image preprocessing. The CIDL-DSSKC technique uses the Xception model to derive a useful set of feature vectors. Besides, the flower pollination algorithm (FPA) is employed to choose parameters linked to the Xception method optimally. For the identification and classification of kidney cancer, the β-variational autoencoder (β-VAE) approach is employed. A renal image dataset containing many images has been used in the experimental outcomes of the CIDL-DSSKC method.

Keywords- *Computational intelligence; Nature-inspired algorithm; Deep learning; Decision support system; Kidney cancer*

I. Introduction

Kidney cancer is a cancer that mostly occurs in men compared to women [1]. Renal cell carcinoma (RCC) is an aggressive and common kind of kidney cancer in patients, especially adults. Annually, about 300,000 people are affected around the world, and it is responsible for more than 100,000 death cases [2]. It grows in the lining of the proximal kidney tubule, whereas tumorous cells grow over time as mass and can be deployed over other organs. Usually, the symptoms of RCC are not easily diagnosed and are hidden. Numerous problems obstruct the classifier of RCC subtypes, such as the absence of an enormous dataset with accurately localized annotation [3]. In addition, there exists a simple data imbalance because the clear cell subtypes include the variation in the appearance of similar subtypes on multiple resolution levels and in most medical cases, and the coherency of RCC cells in various sub-types is also challenging [4]. The current RCC classification framework depends on the valuable annotations of pathology digital slides [5].

Various computational methods were devised to address such challenges for analyzing HPI for diagnosis purposes in multiple tumors [6]. This analysis has relied conventionally on the applications of classification algorithms that process "handcrafted" image-derived features like cell shape, pixel, and size intensity distribution monitored in selected slide patches or full slides [7]. New opportunities have been mounted for the applications of deep learning (DL) approaches with the increasing volume of histology

---

College of Technical Engineering, the Islamic University, Najaf, Iraq

ahmedalkhayyat85@gmail.com

Department of Electrical Engineering, College of Engineering, University of Baghdad, Baghdad 10001, Iraq

ibraheemki@coeng.uobaghdad.edu.iq (corresponding author)

datasets and the wide acceptance of whole-slide high-content imaging [8,9,10,11,12]. Different from the prior generation of machine learning (ML) techniques, DL approaches depend on convolutional neural network (CNN) processing raw intensity images and learning to extract prediction features automatically [13-17]. The potential and accuracy of the DL model to analyze HPI for prognostic and diagnostic purposes have been exposed in many research fields [18]. Therefore, DL could play a prominent role in the era of precision medicine and digital pathology.

The study proposes a Computational Intelligence with Deep Learning Decision Support System for Kidney Cancer (CIDL-DSSKC) technique on renal histopathology images. The presented CIDL-DSSKC technique uses Median and Wiener filters for image preprocessing. The CIDL-DSSKC technique uses the Xception model to derive a useful set of feature vectors. Besides, the flower pollination algorithm (FPA) was leveraged to choose parameters related to the Xception method. For the recognition and detection of kidney cancer, β-variational autoencoder (β-VAE) approach is employed. The outcome study of the CIDL-DSSKC technique is verified utilizing a dataset of renal images.

II. Related Works

In [19], the authors presented a DL technique that mechanically divides the complicated nuclei in histological imageries by applying a potential encoding and decoding structure with an SCPP-Net separable convolutional pyramid-pooling network. The SCPP unit focused on two main characteristics: firstly, it raises the receptive domain by changing four dilation rates, keeps kernel size set, and then lessens trained parameters through depthwise convolution. Zhou et al. [20] introduce a method to inspect the impact of transfer learning (T.L.) on computed tomography (C.T.) scans for malignant and benign detection of renal cancers and, by building patient-level approaches, try to enhance the classifier accuracy. The ImageNet dataset has pre-trained the InceptionV3 model, which was cross-trained to do this classification. Zhu et al. [21] introduced a DNN method to precisely categorize digitized biopsy and surgical resection slides into five relevant classes: chromophobe RCC, clear cell RCC, renal oncocytoma, and papillary RCC.

In [22], the authors devised and evaluated a new DL structure for cancer classification tasks to discriminate papillary and clear cell RCC. This DL structure is made up of 3 CNNs. The author classified whole-slide kidney imagery as patches with three sizes, whereas all networks processed particular patch sizes. Schulz et al. [23] assessed and developed a multimodal DL model (MMDLM) for diagnosis forecasting in ccRCC. The authors [24] presented an end-to-end DL method for diagnosing the five most important histologic sub-types of renal cancers, including both malignant and benign cancers on multi-phase C.T. In [25], the authors developed a new structure (Kidney-SegNet) that combines the efficacy of related encoder and decoder structure with spatial pyramid pooling, including effective dimension-wise convolutional. DiPalma et al. [26] introduced a new DL-related technique to enrich the computation efficacy of histological image classification. This study works at both the slide and tissue level, eliminating the necessity for complex patch-level labeling.

III. Materials And Methods

In this research, we have presented the CIDL-DSSKC system for the identification and detection of kidney cancer on renal imageries. The presented CIDL-DSSKC model studies the renal images for the identification and recognition of kidney cancer. In the presented CIDL-DSSKC approach, many sub-processes were contained, such as image preprocessed, Xception feature removal, FPA-based parameter tuning as well as β-VAE based classification. Fig. 1 demonstrates the entire flow of the CIDL-DSSKC method.

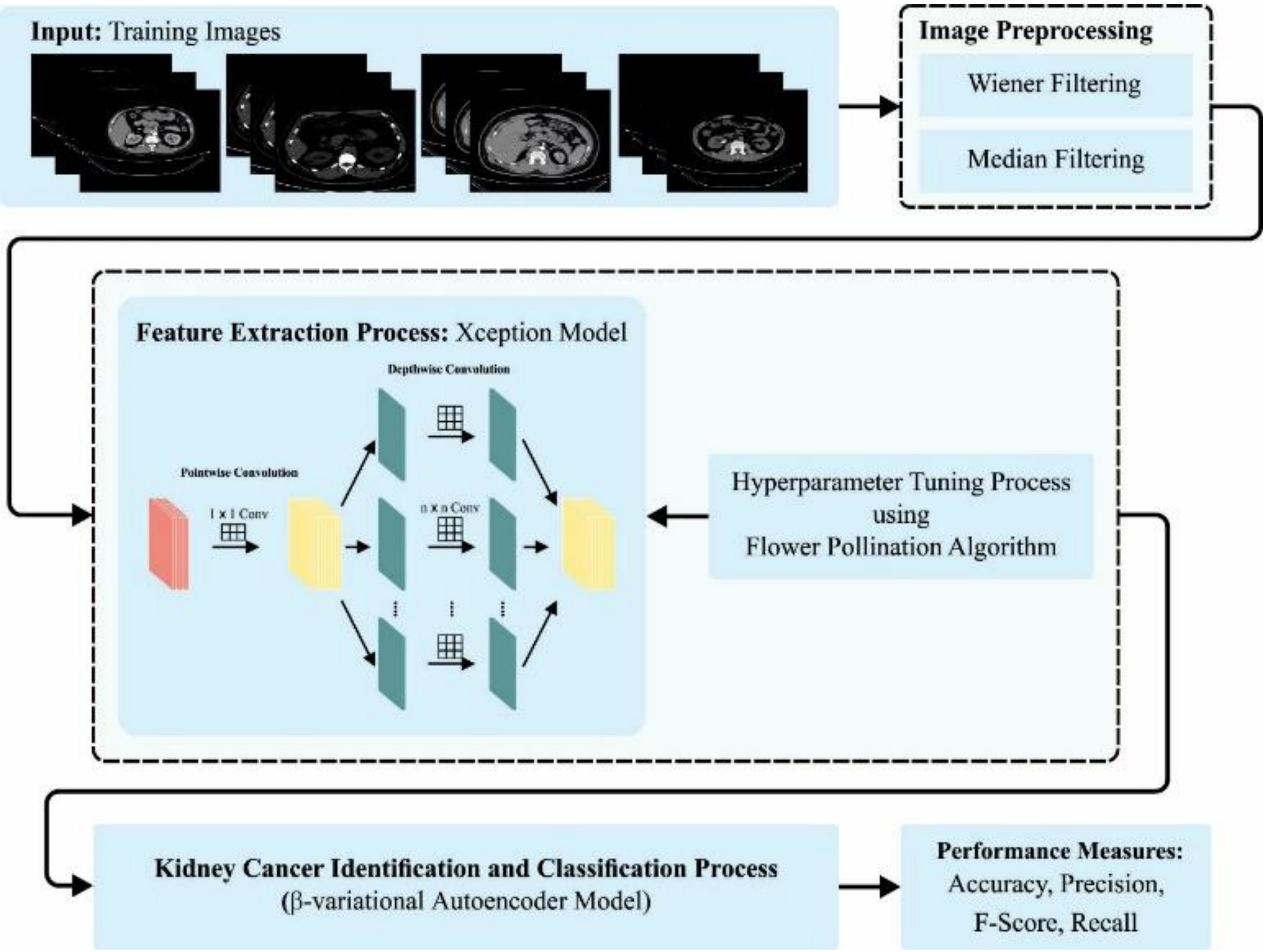

Fig. 1. **The overall flow of the CIDL-DSSKC method**

3.1. Data Used

In this study, kidney cancer classification results of the CIDL-DSSKC system were tested on the C.T. database from the Kaggle repository. The dataset contains 4000 samples with four classes.

3.2. Image Preprocessing

Image preprocessing is performed to optimize the image quality. Generally, the degraded image was prone to noise, is restored by the proper techniques like filtering [27]:

$$g(x,y) = f(x,y)^{*}u(x,y) + n(x,y) \tag{1}$$

$$h(x,y) = R[g(x,y)] \tag{2}$$

In Eq. (1) and (2), $g(x,y)$ indicates the output degraded image, $u(x,y)$ denotes the degradation function, $f(x,y)$ refers to the acquired image, "$*$" shows the convolution, $n(x,y)$ signifies noise namely Gaussian noise, and $h(x,y)$ denotes the concluding output image. The degraded image was inputted to the noise reduction M.F.s and Wiener filter (W.F.s) for obtaining denoised gamma images, a noise reduction filter with a nonlinear spatial domain frequently applied for obtaining denoised images. The procedure to improve the excellence of images is given in the following: Firstly, the mask matrix of $n \times m$ sizes is fixed for the reduction of spatial noise. In contrast with the mask pixel value for tarnished images respective to mask pixel dimensional, the mask matrix is utilized to recalculate the newest pixel value. The median filter modifies all the pixel values to the median pixel value respective to the mask matrix at the central pixel value. The W.F. includes the average pixel and variance values in the $n \times m$ size and is given as follows:

$$m = \frac{1}{NM}\sum_{n,m\in\eta} a\,(n,m) \tag{3}$$

$$\sigma^2 = \frac{1}{NM}\sum_{n,m\in\eta} a^2\,(n,m) - \mu^2 \qquad (4)$$

In Eq. (3) and (4), $a(n,m)$ represents all the pixels in the area η, μ indicates the mean, σ^2 denotes the variance of Gaussian noise, and $n \times m$ shows the size of neighborhood region η in the mask. The W.F. is expressed to the newest pixel that is characterized by $b_w(n,m)$ using the estimated value.

$$b_w(n,m) = \mu + \frac{\sigma^2 - v^2}{\sigma^2} \cdot (a(n,m) - \mu) \qquad (5)$$

In Eq. (5), v^2 denotes the noise variance setting of the mask matrix for the W.F. applications.

3.3. Feature Extraction: Optimal Xception Model

The Xception model is used to produce effectual feature vectors. Xception, an amended version of InceptionV3, is a Depthwise Separable Convolution (Conv) based DNN model [28]. All the input streams are processed utilizing one convolution filter during a Conv procedure called depthwise Conv. A kind of Conv named pointwise Conv exploits a 1x1 kernel that repeats over all the points. The kernel depth corresponds to the number of channels in the source images. A pointwise Conv was merged with depthwise Conv to generate a depthwise Conv layer.

After the depthwise Conv, pointwise Conv takes place in the original depthwise separable Conv layer, and after the pointwise Conv, a depthwise Conv layer takes place in the improved depthwise Conv. The Xception module utilized adapted separable Conv. Separable Conv is the modified depthwise separable Conv, with a remaining connection from the middle flow. Initially, the data passes through the input flow, then passes over the middle flow, and finally, through the exit flow in the Xception module. Average Pooling with the size of 4*4, dense and flattening layers, is added to categorize the images.

This study uses the FPA to choose parameters linked to the Xception approach. FPA is based on the pollination behavior of flowering plants [29]. The key point of this technique is discussed as follows:

Concept 1: the local search (local) can be described by the abiotic and self-pollination in wildlife.

Concept 2: the global search (global pollination) is represented by the biotic and cross-pollination, which depends on Lévy flight. The pollinator bears pollen.

Concept 3: the reproduction probability assumes that the potential solution (flower stability) is equivalent to the similarity of the two flowers.

Concept 4: Global and local pollination can impact any external reason. Thus, the balance among international as well as local pollinations might be controlled by the switching probability $p \in [O,1]$.

Consider a search space $\mathscr{y} = \{s_1, s_2, \ldots, s_{\mathrm{m}}\}$ of potential solutions so that $s_i \in \mathfrak{R}^n$, FPA to resolve the subsequent challenges:

$$s^* = \operatorname{argmin}_{s\epsilon\mathscr{y}}\{f(s)\}, \qquad (6)$$

In Eq. (6), $f(\cdot)$ refers to the "objective function." In general, one could review the FPA working process in 5 stages as follows:

Step 1: Parameter Description.

FPA includes subsequent parameters:

- m: implies the population size (count of flowers or solutions).
- s_{best}: signifies the present optimum solution.
- l: shows the size of the step.
- p: the switching probability that resolves if global or local pollination is subsequently FPA.

Step 2: Population Initialization.

Initialize the decision variable $x \in \mathfrak{x}$ in the random range. One method $\mathfrak{x}$ is represented as a bi-dimension matrix, viz., $\mathfrak{x} \in \mathfrak{R}^{\mathrm{m}\times n}$:

$$FPX = \begin{bmatrix} x_1^1 & x_2^1 & \ldots & x_{\mathrm{n}}^1 \\ x_1^2 & x_2^2 & \ldots & x_{\mathrm{n}}^2 \\ \vdots & \vdots & \ldots & \vdots \\ x_1^m & x_2^m & \ldots & x_{\mathrm{n}}^m \end{bmatrix} \qquad (7)$$

In Eq. (7), $x_{i,j} \in [l_j, u_j]$, so that l_j and u_j Refer to the lower and upper bounds of the j^{th} search space, correspondingly. Each potential solution (the flowers) was initialized by using Eq. (8):

$$x_{i,j} = l_j + (u_j - l_j) \times q, \qquad (8)$$

Where q represents the scalar random number within [0,1]. Based on the F.F. value, The generated solution is stored in $\mathfrak{x}$ in ascending sequence, viz., $(x_1) \le f(x_2) \le \cdots \le f(x_{\mathrm{m}})$. In addition, the global optimum flower s_{best} can be initialized in this way: $s_{best} = x_1$.

Step3: Present flower population Intensification

As mentioned, p determines whether the pollinator follows global or local pollination:

- Abiotic (Local Search): this pollination occurs without a pollinator, viz., the broadcast of pollen relies on the wind and diffusion. The local pollination and flower constancy at r time step was characterized by Eq. (9):

$$s_i^{t+1} = s_i^t + \varepsilon\left(s_j^t - s_c^t\right). \qquad (9)$$

The basis is to mimic the constancy of flowers from the local neighborhood. According to statistical data, s_j^t and s_{k}^t either come from identical species or are selected from the FPA population.

- Global Search (Biotic): the pollen of flowers can be transferred long-distance via pollinators such as bees, bats, birds, and so on. This ensures that reproduction and pollination are the most suitable. The biotic FPA procedure can be represented as follows:

$$x_i^{t+1} = x_i^t + L(x_{best} - x_i^t). \qquad (10)$$

While insects could travel long distances with dissimilar step sizes, Lévy flight can be used to effectively imitate these characteristics. Thus, the representation of $\mathrm{L} > 0$ from the Levy distribution is expressed as follows:

$$L \sim \frac{\lambda\Gamma(\lambda)\sin\left(\frac{\pi\lambda}{2}\right)}{\pi}\frac{1}{Q^{1+\lambda}}, \qquad (11)$$

In Eq. (11), $\Gamma(\lambda)$ represents the gamma function that is larger steps $(Q"s_0 > 0)$. Here, it is fixed $\lambda = 1.5$.

Step 4: FPA Upgrading with global optimum flower.

The optimum flower s_{best} was upgraded for all the iterations t if $f(s_i^t) < f(s_{best}), \forall i = 1,2,\ldots,m.$

Step 5: Stopping condition.

FPA iterates steps 3 and 4 until the ending criteria (the iteration number or the quality of the result) is satisfied.

Fitness choice is a main problem of BSA. An encoder result is used to estimate the best solution candidate. Here, the exactness value is a major state applied to strategy F.F.

$$Fitness = \max(P) \qquad (12)$$

$$P = \frac{TP}{TP + FP} \qquad (13)$$

Where TP and FP imply true and false positive values.

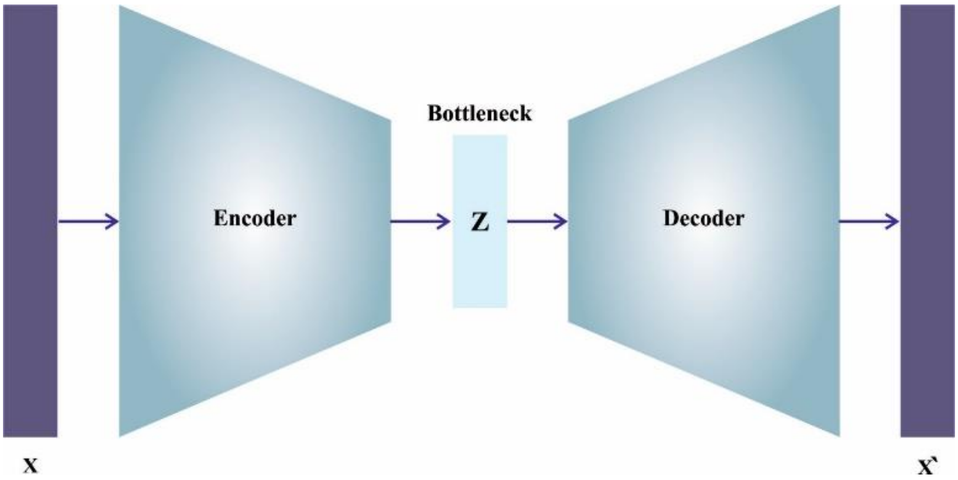

Fig. 2. **Structure of VAE**

3.4. Image Classification: β –VAE Model

Finally, the classification of kidney cancer takes place utilizing the β-VAE method. VAE is the generative mechanism that comprises encoding and decoding parts, and the aim is to increase the marginal probability of the reconstruction output that is shown below [30, 31, 32, 33]:

$$log_{p_\theta}(X) \geq E_{Z\sim q_\varphi(Z|X)}[logp_\theta(X|Z)] - D_{KL}\left(q_\varphi(Z|X)\|p(Z)\right) \qquad (14)$$

Here, the initial period is the log probability that input X is produced 0by the sampled Z in inferred distribution, $q_{\phi}(Z|X)$. This distribution was considered to follow the multivariate standard distribution. The substructure of VAE is demonstrated in Fig. 2.

The loss function of VAE comprises a 1st period that fines the reconstructed error among the inputs and outputs and a 2nd term that forces the learned distribution, $q_{\varphi}(Z|X)$, to be the same for the prior distribution, $p(Z)$:

$$\mathcal{L}_{VAE}(\theta,\varphi)=\mathcal{L}_{recon}(\theta,\varphi)+\mathcal{L}_{KL}(\theta,\varphi), \qquad (15)$$

Where the reconstruction loss, $\mathcal{L}_{recon}(\theta,(\theta,\varphi))$, and the K.L. loss, $\mathcal{L}_{KL}(\theta,(\theta,\varphi))$, are evaluated by the following expression:

$$\mathcal{L}_{recon}(\theta,(\theta,\varphi)) = \sum_{i=1}^{N}\|\hat{X} - X\|_{2}^{2}, \qquad (16)$$

$$\mathcal{L}_{KL}(\theta,(\theta,\varphi)) = D_{KL}(q_{\varphi})((Z|X)\|p\,(Z)) \qquad (17)$$

Here, $\beta - VAE$ has demonstrated better performance based on multiple disentanglement metrics, and it is used as a backbone of this model for encouraging the disentanglement as it is easier to express.

The $\beta - VAE$ method is an extension of typical VAE that aim is to acquire the disentangled representation of the encoder variable in an unsupervised way by providing additional weight to the KL term than original VAE, with extra hyperparameter β:

$$\mathcal{L}_{VAE}(\theta,\varphi) = \mathcal{L}_{recon}(\theta,\varphi) + \beta\mathcal{L}_{KL}(\theta,\varphi), \qquad (18)$$

IV. RESULTS AND DISCUSSION

In this study, kidney cancer recognition results of the CIDL-DSSKC approach are verified on C.T. datasets from the Kaggle repository [34]. The dataset has 4000 instances with four class labels, as shown in Table 1.

TABLE I. **DETAILS OF DATABASE**

Classes	**No. of Samples**
Normal	1000
Cyst	1000
Tumor	1000
Stone	1000
Total Number of Samples	4000

The confusion matrices of the CIDL-DSSKC method are shown in Fig. 3. The outcomes showed that the CIDL-DSSKC technique identifies four classes competently. In Table 2 and Fig. 4, kidney cancer outcomes of the CIDL-DSSKC method are obviously demonstrated at 80:20 of Training phase (TRPH)/ Testing phase (TSPH). The experimental value identified that the CIDL-DSSKC model attained improved outcomes. On 80% of TRPH, the CIDL-DSSKC model gains average $accu_y$, $prec_n$, $reca_l$, and F_{score} of 98.33%, 96.65%, 96.66%, and 96.65% respectively. Also, on 20% of TRPH, the CIDL-DSSKC method gains average $accu_y$, $prec_n$, $reca_l$, and F_{score} of 97.81%, 95.61%, 95.54%, and 95.56% correspondingly.

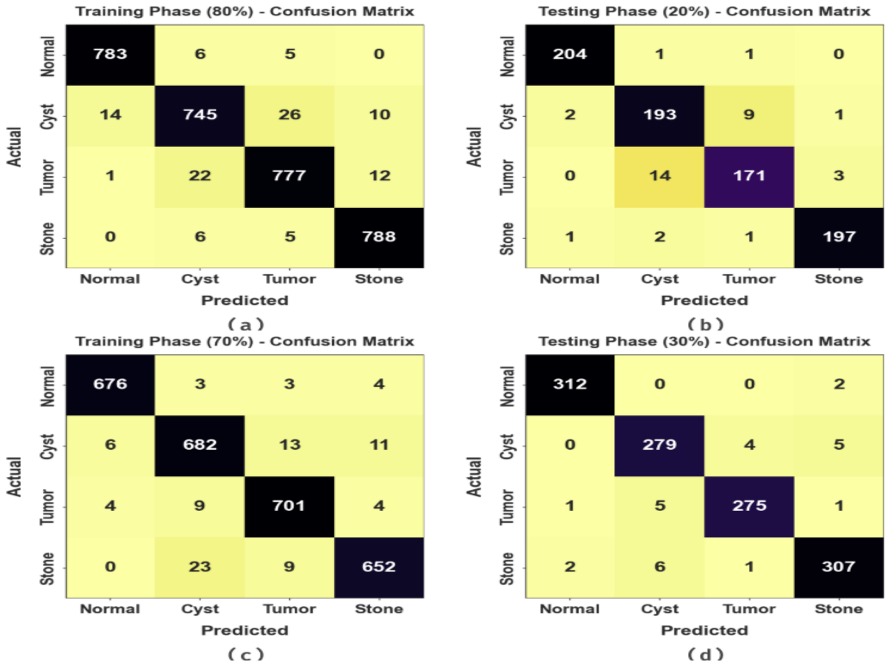

Training Phase (80%) - Confusion Matrix

Actual \ Predicted	Normal	Cyst	Tumor	Stone
Normal	783	6	5	0
Cyst	14	745	26	10
Tumor	1	22	777	12
Stone	0	6	5	788

(a)

Testing Phase (20%) - Confusion Matrix

Actual \ Predicted	Normal	Cyst	Tumor	Stone
Normal	204	1	1	0
Cyst	2	193	9	1
Tumor	0	14	171	3
Stone	1	2	1	197

(b)

Training Phase (70%) - Confusion Matrix

Actual \ Predicted	Normal	Cyst	Tumor	Stone
Normal	676	3	3	4
Cyst	6	682	13	11
Tumor	4	9	701	4
Stone	0	23	9	652

(c)

Testing Phase (30%) - Confusion Matrix

Actual \ Predicted	Normal	Cyst	Tumor	Stone
Normal	312	0	0	2
Cyst	0	279	4	5
Tumor	1	5	275	1
Stone	2	6	1	307

(d)

Fig. 3. **Confusion matrices of CIDL-DSSKC method (a-b) 80:20 of TRPH/TSPH and (c-d) 70:30 of TRPH/TSPH**

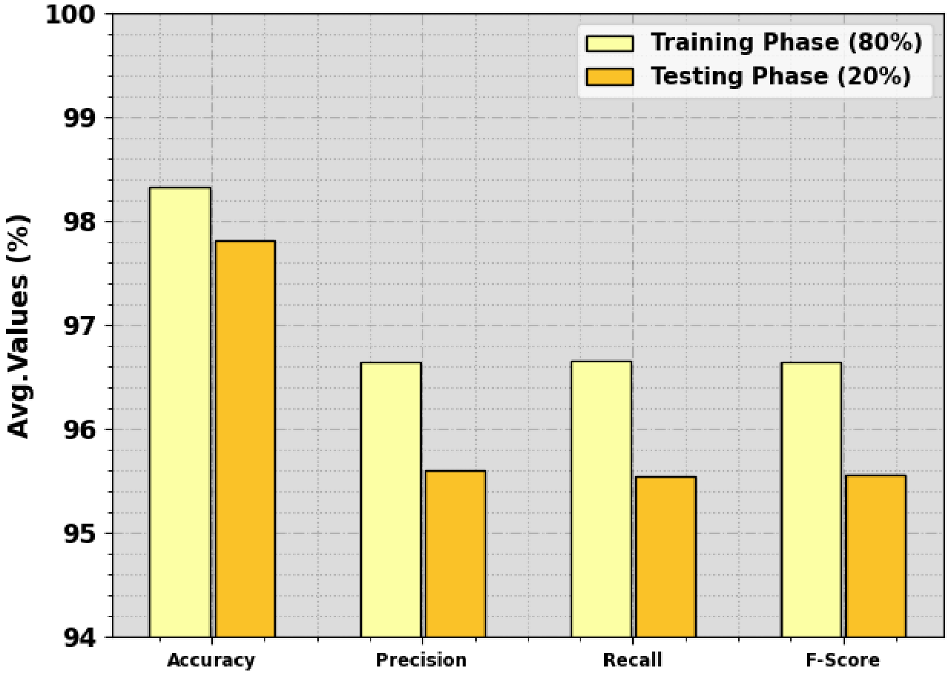

Fig. 4. **Average outcomes of CIDL-DSSKC approach on 80:20 of TRPH/TSPH**

TABLE II. **KIDNEY CANCER OUTCOMES OF CIDL-DSSKC METHOD ON 80:20 OF TRPH/TSPH**

Classes	$\boldsymbol{Accu_y}$	$\boldsymbol{Prec_n}$	$\boldsymbol{Reca_l}$	$\boldsymbol{F_{score}}$
Training Phase (80%)				
Normal	99.19	98.12	98.61	98.37
Cyst	97.38	95.64	93.71	94.66
Tumor	97.78	95.57	95.69	95.63
Stone	98.97	97.28	98.62	97.95
Average	**98.33**	**96.65**	**96.66**	**96.65**
Testing Phase (20%)				
Normal	99.38	98.55	99.03	98.79
Cyst	96.37	91.90	94.15	93.01
Tumor	96.50	93.96	90.96	92.43
Stone	99.00	98.01	98.01	98.01
Average	**97.81**	**95.61**	**95.54**	**95.56**

Fig. 5 investigates the $accu_y$ of the CIDL-DSSKC technique during the training and validation on 80:20 of TRPH/TSPH. The figure displays that the CIDL-DSSKC model obtains the highest $accu_y$ values over increasing epochs. Also, the maximum validation $accu_y$ overtraining $accu_y$ shows that the CIDL-DSSKC system learns efficiently on 80:20 of TRPH/TSPH. The loss analysis of the CIDL-DSSKC technique during training and validation is illustrated at 80:20 TRPH/TSPH in Fig. 6. The outcome shows that the CIDL-DSSKC methodology accomplishes the nearby values of training and validation loss. The CIDL-DSSKC method gains proficiently on 80:20 of TRPH/TSPH. A brief P.R. analysis of the CIDL-DSSKC model is illustrated at 80:20 TRPH/TSPH in Fig. 7. The outcome stated that the CIDL-DSSKC technique has an impact on the growing values of P.R. Furthermore, the CIDL-DSSKC method could attain maximum P.R. values on all class labels. In Fig. 8, an ROC research of the CIDL-DSSKC system is shown at 80:20 TRPH/TSPH. The figure reported that the CIDL-DSSKC method resulted in enhanced ROC values. The CIDL-DSSKC system can also range superior ROC values in all classes. In Table 3 and Fig. 9, the kidney cancer outcome of the CIDL-DSSKC method is clearly illustrated at 70:30 TRPH/TSPH. The experimental outcomes showed that the CIDL-DSSKC method obtained superior outcomes. On 70% of TRPH, CIDL-DSSKC methodology reaches average $accu_y$, $prec_n$, $reca_l$, and F_{score} of 98.41%, 96.85%, 96.82%, and 96.83% correspondingly. Also, on 30% of TRPH, the CIDL-DSSKC system attains average $accu_y$, $prec_n$, $reca_l$, and F_{score} of 98.87%, 97.73%, 97.73%, and 97.73% correspondingly. Fig. 10 examines the $accu_y$ of CIDL-DSSKC model at training and validation process on 70:30 of TRPH/TSPH. The figure indicates that the CIDL-DSSKC method gains the highest $accu_y$ values over increasing epochs. Also, the maximum validation $accu_y$ overtraining $accu_y$ Illustrates that CIDL-DSSKC methodology learns efficiently on 70:30 of TRPH/TSPH.

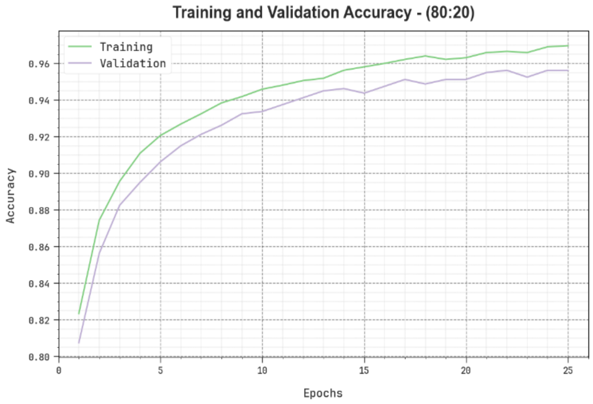

Fig. 5. **Accuracy curve of CIDL-DSSKC approach on 80:20 of TRPH/TSPH**

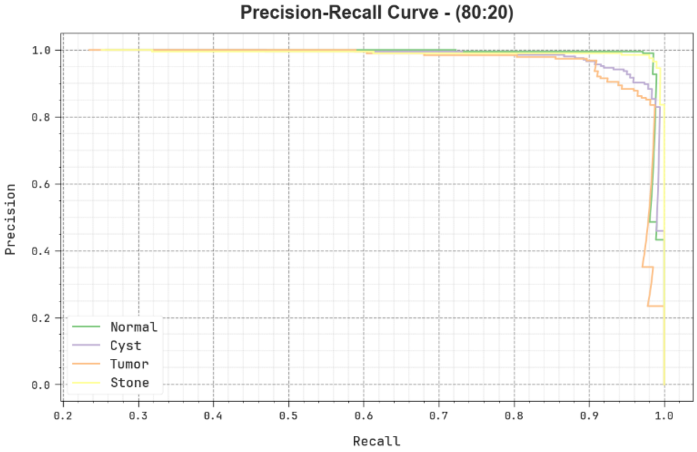

Fig. 6. **Loss curve of CIDL-DSSKC method on 80:20 of TRPH/TSPH**

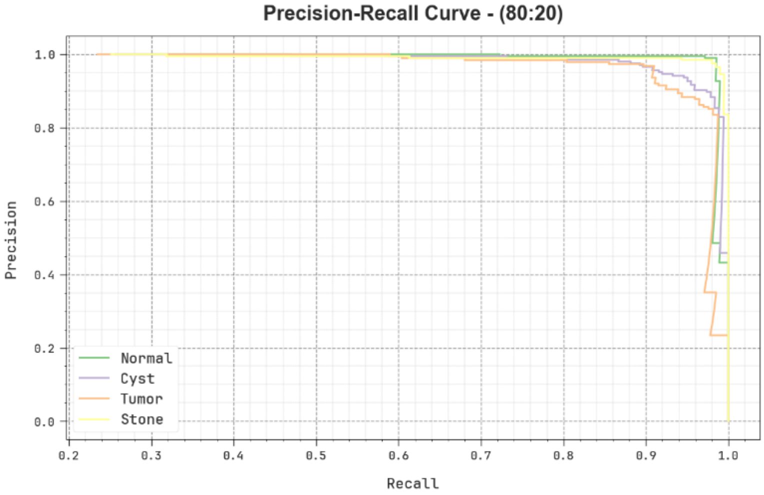

Fig. 7. **PR curve of CIDL-DSSKC approach on 80:20 of TRPH/TSPH**

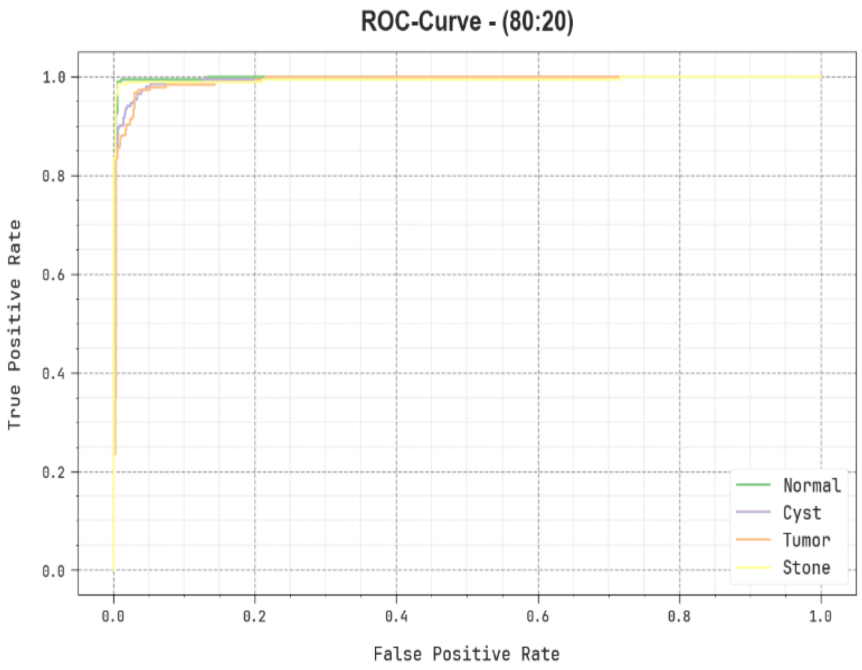

Fig. 8. **ROC curve of CIDL-DSSKC approach on 80:20 of TRPH/TSPH**

TABLE III. **KIDNEY CANCER OUTCOMES OF CIDL-DSSKC METHOD ON 70:30 OF TRPH/TSPH**

Classes	$Accu_y$	$Prec_n$	$Reca_l$	F_{score}
Training Phase (70%)				
Normal	99.29	98.54	98.54	98.54
Cyst	97.68	95.12	95.79	95.45
Tumour	98.50	96.56	97.63	97.09
Stone	98.18	97.17	95.32	96.24
Average	**98.41**	**96.85**	**96.82**	**96.83**
Testing Phase (30%)				
Normal	99.58	99.05	99.36	99.21
Cyst	98.33	96.21	96.88	96.54
Tumor	99.00	98.21	97.52	97.86
Stone	98.58	97.46	97.15	97.31
Average	**98.87**	**97.73**	**97.73**	**97.73**

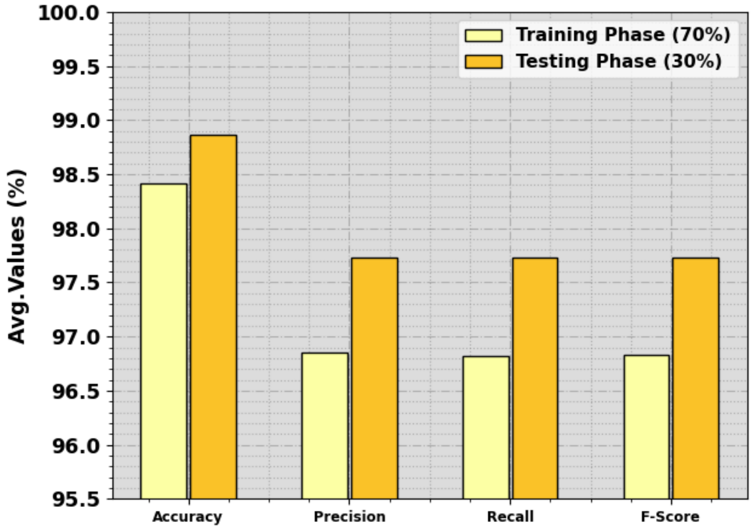

Fig. 9. **Average outcomes of the CIDL-DSSKC approach on 70:30 of TRPH/TSPH**

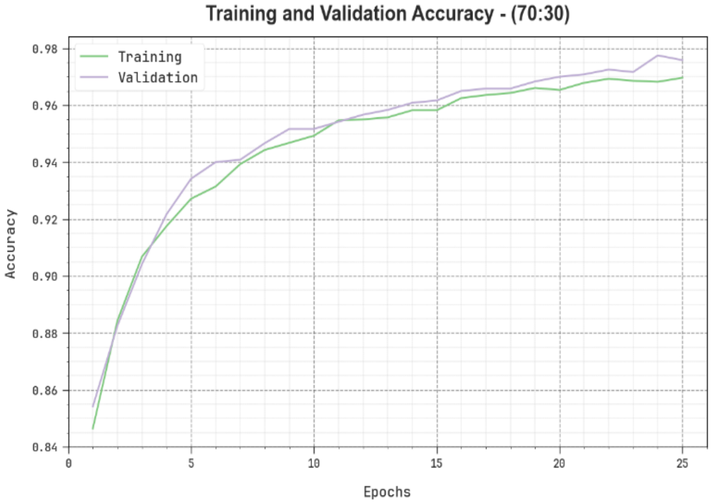

Fig. 10. **Accuracy curve of CIDL-DSSKC approach on 70:30 of TRPH/TSPH**

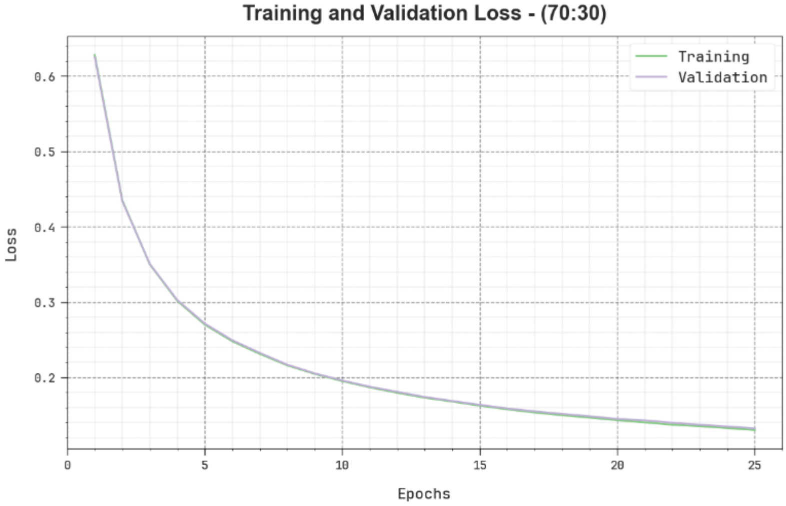

Fig. 11. **Loss curve of CIDL-DSSKC method on 70:30 of TRPH/TSPH**

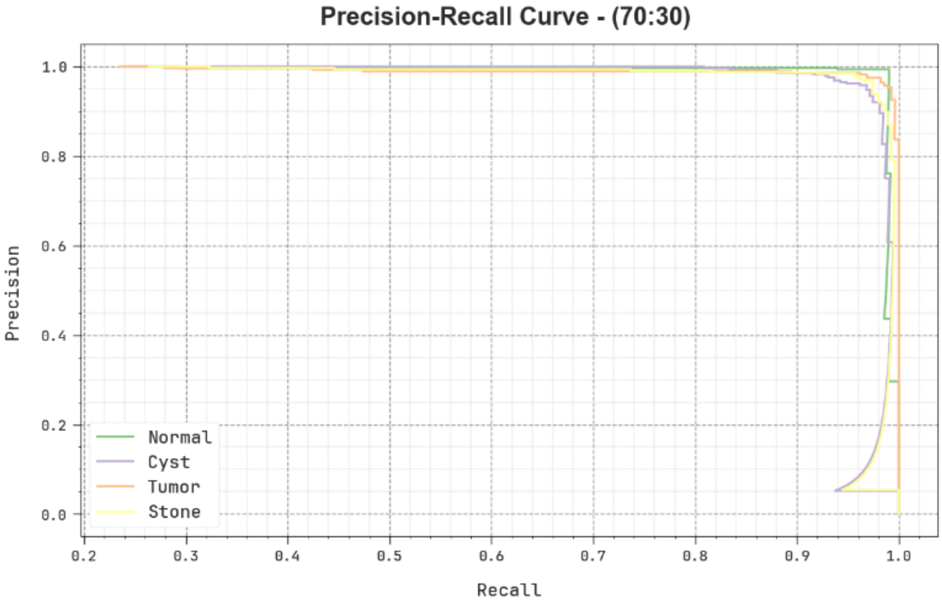

Fig. 12. **PR curve of CIDL-DSSKC approach on 70:30 of TRPH/TSPH**

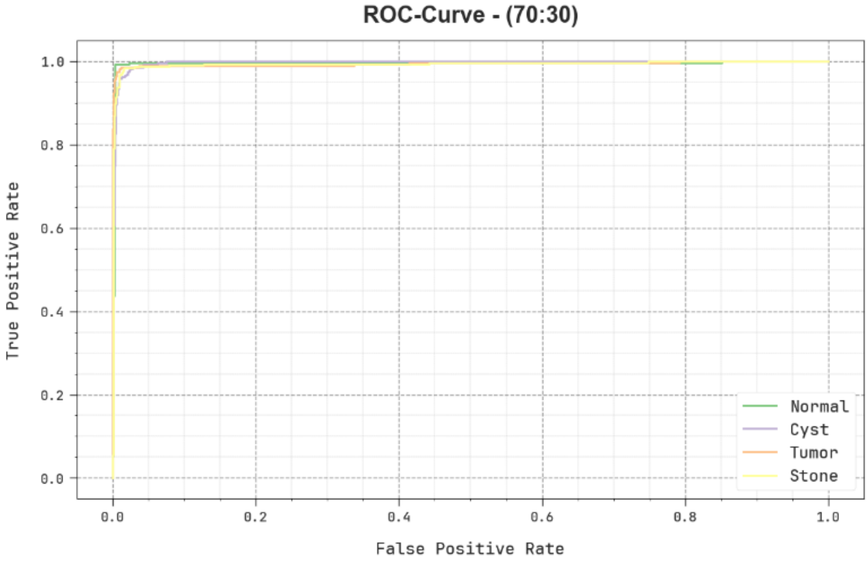

Fig. 13. **ROC curve of CIDL-DSSKC approach on 70:30 of TRPH/TSPH**

The loss analysis of the CIDL-DSSKC method at training and validation is illustrated on 70:30 of TRPH/TSPH in Fig. 11. The result represents that the CIDL-DSSKC methodology obtains nearby values of training and validation loss. The CIDL-DSSKC system learns effectively at 70:30 of TRPH/TSPH. A brief P.R. curve of the CIDL-DSSKC technique is demonstrated at 70:30 for TRPH/TSPH in Fig. 12 and 13. The outcomes stated that the CIDL-DSSKC technique outcomes in maximum values of P.R. Moreover, the CIDL-DSSKC method attains maximum P.R. values in all classes. In Fig. 14, an ROC analysis of the CIDL-DSSKC method is reported at 70:30 TRPH/TSPH. The figure defined that the CIDL-DSSKC system resulted in superior ROC values. Moreover, the CIDL-DSSKC method can range superior ROC values on all classes.

The experimental results of the CIDL-DSSKC technique are compared with existing techniques in Table 4 and Fig. 14 [35]. These outcomes show that VGG16 and Adaboost methods demonstrate worse outcomes than other models. Next, the CNN-4 model exhibits slightly improved results. At the same time, the CNN-6, CNN-4, Inception v3, and 2D-CNN models offer moderately enhanced performance. But the CIDL-DSSKC technique demonstrated better results with $accu_y$, $prec_n$, $reca_l$, and F_{score} of 98.87%, 97.73%, 97.73%, and 97.73%. Therefore, the CIDL-

DSSKC method can be applied for automated kidney cancer detection.

TABLE I. **COMPARATIVE OUTCOME OF THE CIDL-DSSKC METHOD WITH OTHER EXISTING TECHNIQUES**

Models	**Accuracy**	**Precision**	**Recall**	**F-Score**
VGG16	60.00	83.62	73.55	80.11
ResNet50	96.00	92.80	93.66	94.12
CNN-6	97.00	91.76	93.91	92.06
CNN-4	92.00	92.10	93.39	90.81
InceptionV3	97.00	95.84	94.31	90.91
AdaBoost	75.00	90.44	94.12	90.49
2D-CNN	97.00	90.66	90.12	93.88
CIDL-DSSKC	98.87	97.73	97.73	97.73

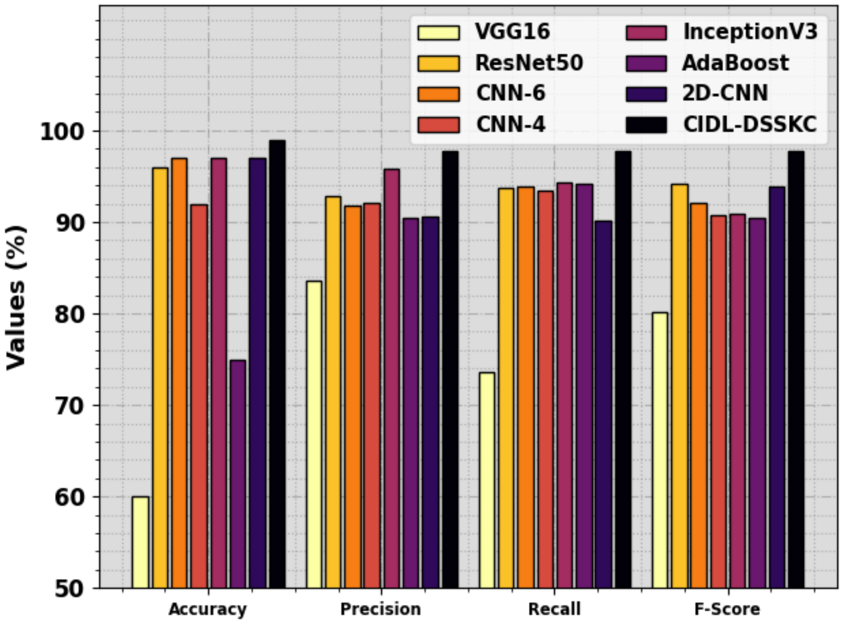

Fig. 14. **Comparative outcome of CIDL-DSSKC method with other existing techniques**

V. Conclusion

In this study, we presented the Computational Intelligence with Deep Learning Decision Support System for Kidney Cancer (CIDL-DSSKC) on renal images, which integrates Median and Wiener filters for image preprocessing, the Xception model for feature extraction, and the β-Variational Autoencoder (β-VAE) for classification. Our experimental results, conducted on a C.T. dataset from the Kaggle repository with 4000 samples across four classes (Normal, Cyst, Tumor, and Stone), demonstrated the effectiveness of the CIDL-DSSKC approach. The CIDL-DSSKC model achieved an average accuracy of 98.33%, precision of 96.65%, recall of 96.66%, and F1-score of 96.65% during the training phase (80% of the dataset). In the testing phase (20% of the dataset), the model attained an average accuracy of 97.81%, precision of 95.61%, recall of 95.54%, and F1-score of 95.56%. These results indicate that the CIDL-DSSKC model can accurately and efficiently classify kidney cancer types, providing radiologists with a reliable decision-support tool. The findings of this study suggest that the proposed method not only enhances diagnostic accuracy but also reduces the time and effort required for manual analysis, potentially improving patient outcomes. Compared to traditional methods, our approach offers a more robust and automated solution for kidney cancer detection. Future research could further optimize the model's parameters, incorporate larger and more diverse datasets, and explore integrating other advanced deep learning techniques to improve classification performance. Our study lays a solid foundation for the development of more sophisticated and comprehensive diagnostic tools in the field of medical imaging.

Declarations of interest: the authors declare that they have no conflict of interest.

Data Availability: "N/A".

Conflict of interest: The authors declare no conflict of interest.

Acknowledgments: The authors would like to acknowledge the support of Prince Sultan University in paying the Article Processing Charges (APC) for this publication. Special acknowledgment to Automated Systems and Soft Computing Lab (ASSCL), Prince Sultan University, Riyadh, Saudi Arabia. In addition, the authors wish to acknowledge the editor and anonymous reviewers for their insightful comments, which have improved the quality of this publication.

References

[1] F. Hao, X. Liu, M. Li, and W. Han, "Accurate kidney pathological image classification method based on deep learning and multimodal fusion method with application to membranous nephropathy," Life, vol. 13, no. 2, p. 399, 2023.

[2] J. Noorbakhsh, S. Farahmand, A. Foroughi Pour, S. Namburi, D. Caruana, D. Rimm, M. Soltanieh-Ha, K. Zarringhalam, and J.H. Chuang, "Deep learning-based cross-classifications reveal conserved spatial behaviors within tumor histological images," Nature Communications, vol. 11, no. 1, p. 6367, 2020.

[3] E. Marostica, R. Barber, T. Denize, I.S. Kohane, S. Signoretti, J.A. Golden, and K.H. Yu, "Development of a histopathology informatics pipeline for classification and prediction of clinical outcomes in subtypes of renal cell carcinoma-integrative pathology-genomics analysis for renal cancers," Clinical Cancer Research, vol. 27, no. 10, pp. 2868-2878, 2021.

[4] S. Tabibu, P.K. Vinod, and C.V. Jawahar, "Pan-renal cell carcinoma classification and survival prediction from histopathology images using deep learning," Scientific Reports, vol. 9, no. 1, pp. 1-9, 2019.

[5] E. Wulczyn, D.F. Steiner, Z. Xu, A. Sadhwani, H. Wang, I. Flament-Auvigne, C.H. Mermel, P.H.C. Chen, Y. Liu, and M.C. Stumpe, "Deep learning-based survival prediction for multiple cancer types using histopathology images," PloS One, vol. 15, no. 6, p. e0233678, 2020.

[6] Jiao, Y., Li, J., Qian, C. and Fei, S., 2021. Deep learning-based tumor microenvironment analysis in colon adenocarcinoma histopathological whole-slide images. Computer Methods and Programs in Biomedicine, 204, p.106047.

[7] Jang, H.J., Lee, A., Kang, J., Song, I.H. and Lee, S.H., 2020. Prediction of clinically actionable genetic alterations from colorectal cancer histopathology images using deep learning. World Journal of Gastroenterology, 26(40), p.6207.

[8] Kers, J., Bülow, R.D., Klinkhammer, B.M., Breimer, G.E., Fontana, F., Abiola, A.A., Hofstraat, R., Corthals, G.L., Peters-Sengers, H., Djudjaj, S. and von Stillfried, S., 2022. Deep learning-based classification of kidney transplant pathology: a retrospective, multicentre, proof-of-concept study. The Lancet Digital Health, 4(1), pp.e18-e26.

[9] M. H. Almusawy, "Improved Arithmetic Optimization with Deep Learning-Driven Traffic Congestion Control for Intelligent Transportation Systems in Smart Cities," Journal of Smart Internet of Things, vol. 2022, no. 1, 2022.

[10] P. Jha, B. Kumar, A. Mishra, V. Ujjwal, A. Singh, "Blockchain-Based Smart Home Network Security through ML," Journal of Smart Internet of Things, vol. 2022, no. 1, 2022.

[11] P. J., R. Kundu, M. K. Bagaria, Y. S. Rajawat, P. Punia, "Blockchain-Based Smart Home Network Security through ML," Journal of Smart Internet of Things, vol. 2023, no. 2, 2023.

[12] W. Alkaberi and F. Assiri, "Predicting the Number of Software Faults using Deep Learning", Eng. Technol. Appl. Sci. Res., vol. 14, no. 2, pp. 13222–13231, Apr. 2024.

[13] Lin, F., Ma, C., Xu, J., Lei, Y., Li, Q., Lan, Y., Sun, M., Long, W. and Cui, E., 2020. A CT-based deep learning model for predicting the nuclear grade of clear cell renal cell carcinoma. European Journal of Radiology, 129, p.109079.

[14] Ohe, C., Yoshida, T., Amin, M.B., Uno, R., Atsumi, N., Yasukochi, Y., Ikeda, J., Nakamoto, T., Noda, Y., Kinoshita, H. and Tsuta, K., 2023. Deep learning-based predictions of clear and eosinophilic phenotypes in clear cell renal cell carcinoma. Human Pathology, 131, pp.68-78.

[15] Anter AM, Hassanien AE, Abu ElSoud M, Azar AT (2015) Automatic Liver Parenchyma Segmentation System from Abdominal CT Scans using Hybrid Techniques. Int. J. Biomedical Engineering and Technology, 17(2): 148-168.

[16] Jothi G, Inbarani HH, Azar AT (2013). Hybrid Tolerance Rough Set: PSO Based Supervised Feature Selection for Digital Mammogram Images. International Journal of Fuzzy System Applications (IJFSA), 3(4), 15-30.

[17] Jothi G., Inbarani HH, Azar AT & Devi K.R. (2019) Rough set theory with Jaya optimization for acute lymphoblastic leukemia classification. Neural Computing and Applications, 31(9): 5175-5194.

[18] Banu PKN, Azar AT, Inbarani HH (2017). Fuzzy firefly clustering for tumor and cancer analysis. Int. J. Modelling, Identification and Control (IJMIC), 27(2): 92-103

[19] Chanchal, A.K., Kumar, A., Lal, S. and Kini, J., 2021. Efficient and robust deep learning architecture for segmentation of kidney and breast histopathology images. Computers & Electrical Engineering, 92, p.107177.

[20] Zhou, L., Zhang, Z., Chen, Y.C., Zhao, Z.Y., Yin, X.D. and Jiang, H.B., 2019. A deep learning-based radiomics model for differentiating benign and malignant renal tumors. Translational oncology, 12(2), pp.292-300.

[21] Zhu, M., Ren, B., Richards, R., Suriawinata, M., Tomita, N. and Hassanpour, S., 2021. Development and evaluation of a deep neural network for histologic classification of renal cell carcinoma on biopsy and surgical resection slides. Scientific reports, 11(1), pp.1-9.

[22] Abdeltawab, H.A., Khalifa, F.A., Ghazal, M.A., Cheng, L., El-Baz, A.S. and Gondim, D.D., 2022. A deep learning framework for automated classification of histopathological kidney whole-slide images. Journal of Pathology Informatics, 13, p.100093.

[23] Schulz, S., Woerl, A.C., Jungmann, F., Glasner, C., Stenzel, P., Strobl, S., Fernandez, A., Wagner, D.C., Haferkamp, A., Mildenberger, P. and Roth, W., 2021. Multimodal deep learning for prognosis prediction in renal cancer. Frontiers in oncology, 11, p.788740.

[24] Uhm, K.H., Jung, S.W., Choi, M.H., Shin, H.K., Yoo, J.I., Oh, S.W., Kim, J.Y., Kim, H.G., Lee, Y.J., Youn, S.Y. and Hong, S.H., 2021. Deep learning for end-to-end kidney cancer diagnosis on multi-phase abdominal computed tomography. NPJ precision oncology, 5(1), p.54.

[25] Aatresh, A.A., Yatgiri, R.P., Chanchal, A.K., Kumar, A., Ravi, A., Das, D., Raghavendra, B.S., Lal, S. and Kini, J., 2021. Efficient deep learning architecture with dimension-wise pyramid pooling for nuclei segmentation of histopathology images. Computerized Medical Imaging and Graphics, 93, p.101975.

[26] DiPalma, J., Suriawinata, A.A., Tafe, L.J., Torresani, L. and Hassanpour, S., 2021. Resolution-based distillation for efficient histology image classification. Artificial Intelligence in Medicine, 119, p.102136.

[27] Park, C.R., Kang, S.H. and Lee, Y., 2020. Median modified wiener filter for improving the image quality of gamma camera images. Nuclear Engineering and Technology, 52(10), pp.2328-2333.

[28] Chollet, F. Xception: Deep learning with depthwise separable convolutions. In Proceedings of the IEEE Conference on Computer Vision and Pattern Recognition, Honolulu, HI, USA, 21–26 July 2017; pp. 1800–1807.

[29] Alkareem Alyasseri, Z.A., Al-Betar, M.A., Awadallah, M.A., Makhadmeh, S.N., Abasi, A.K., Doush, I.A. and Alomari, O.A., A hybrid flower pollination with b-hill climbing algorithm for global optimization. J. King Saud Univ.-Comput. Inf. Sci. doi, 10.

[30] Cetin, I., Stephens, M., Camara, O. and Ballester, M.A.G., 2023. Attri-VAE: Attribute-based interpretable representations of medical images with variational autoencoders. Computerized Medical Imaging and Graphics, 104, p.102158.

[31] Hameed, U., Ur Rehman, M., Rehman, A., Damaševičius, R., Sattar, A., & Saba, T. (2023). A deep learning approach for liver cancer detection in C.T. scans. Computer Methods in Biomechanics and Biomedical Engineering: Imaging & Visualization, 11(7). https://doi.org/10.1080/21681163.2023.2280558

[32] S. Al-Otaibi, M. Mujahid, A. R. Khan, H. Nobanee, J. Alyami and T. Saba, "Dual Attention Convolutional AutoEncoder for Diagnosis of Alzheimer's Disorder in Patients Using Neuroimaging and MRI Features," in IEEE Access, vol. 12, pp. 58722-58739, 2024, doi: 10.1109/ACCESS.2024.3390186.

[33] S. R. Waheed, N. M. Suaib, M. S. M. Rahim, A. R. Khan, S. A. Bahaj and T. Saba, "Synergistic Integration of Transfer Learning and Deep Learning for Enhanced Object Detection in Digital Images," in IEEE Access, vol. 12, pp. 13525-13536, 2024, doi: 10.1109/ACCESS.2024.3354706.

[34] https://www.kaggle.com/datasets/nazmul0087/ct-kidney-dataset-normal-cyst-tumor-and-stone

[35] Alzu'bi, D., Abdullah, M., Hmeidi, I., AlAzab, R., Gharaibeh, M., El-Heis, M., Almotairi, K.H., Forestiero, A., Hussein, A.M. and Abualigah, L., 2022. Kidney Tumor Detection and Classification Based on Deep Learning Approaches: A New Dataset in C.T. Scans. Journal of Healthcare Engineering, 2022.